



erage of unoptimized pre-trained features the optimal OCC optimization objective? What defines a good optimization objective? These questions remain unexplored and theoretically unexplained. Thus, this paper delves into the OCC method’s optimization objective, specifically the center of the hypersphere, and focuses on the following questions:

- What theoretical model should be employed to comprehensively describe the optimization objective of OCC?
- What properties should the OCC optimization objective have to better separate positive and negative samples for better accuracy?
- Can the use of pre-trained feature averages in previous methods be explained by such theory?
- Is there a better strategy for setting the OCC optimization objective beyond the pre-trained average?

In this study, based on the above questions, we deeply explore the impact of the optimization objective of OCC. Through rigorous theoretical analysis and derivation, we draw the following conclusions and contributions:

- The optimization objective of OCC can be represented in polar coordinates. Feature norm (radius) and similarity (angular) are the two crucial factors.
- The polar coordinate space’s ability to discriminate between positive and negative samples hinges on reasonable norm values of OCC optimization objective. Inappropriate norm values can lead to significant degradation of the discrimination performance.
- The common practice of using pre-trained feature averages aligns with this mathematical model.
- Any space with a suitable norm can serve as the optimization objective for OCC model, independent of data.

Elaborations on theoretical derivations and empirical validations are provided in Sections 3, 4, and 5. Moreover, the fourth discovery prompts us to consider the feasibility of employing a data-independent random space as the optimization objective. Consequently, the necessity for pre-trained feature averages predicated on training samples is obviated, allowing for training without the need for initial dataset accumulation. This groundbreaking insight births a data-agnostic deep one-class classification paradigm, thus laying the foundation for propelling traditional offline OCC methods into the realm of online detection. This methodology employs a single  $1 \times 1$  convolutional layer as a trainable projector and utilizes spaces with suitable norms as optimization objectives. Extensive experiments validate our findings’ authenticity and emphasize our approach’s effectiveness, resulting in notable performance advancements across one-class anomaly detection and industrial vision anomaly detection and segmentation tasks.

## 2 Related Work

**Pre-trained based OCC methods:** Traditional OCC methods like OC-SVM (Schölkopf et al. 1999) and SVDD (Tax and Duin 2004) rely on handcrafted features and kernel

functions for mapping features to hyperplanes or hyperspheres. The integration of deep learning has improved feature extraction and mapping. Common deep feature extractors fall into two categories: reconstruction-based networks like Auto-Encoders and pre-trained backbones from large datasets like ImageNet (Deng et al. 2009). However, reconstruction-based networks (e.g., Deep SVDD (Ruff et al. 2018)) often provide compressed, low-resolution, and lossy features, which aren’t ideal for anomaly detection.

To enhance feature quality, more OCC methods adopt pre-trained backbones. These methods transfer or adapt pre-trained features to OCC optimization spaces (e.g., averaged pre-trained features). PANDA (Reiss et al. 2021) employs the continual learning strategy to mitigate pattern collapse issues. MS (Reiss and Hoshen 2023) proposes mean-shifted contrastive loss for better adaptation and provides some exploration of the optimization space of OCC by normalizing pre-trained features (subsequent experiments validate it is a potential solution or instance within our theoretical model). While these methods achieve remarkable results, most lack theoretical exploration of the optimization space, which we believe plays a pivotal role in performance. By exploring this space, we aim to derive theoretical principles, explain the use of pre-trained feature averages, and identify better optimization spaces.

**Anomaly Detection and Segmentation in Industrial Vision:** Compared to OCC tasks, this task is more of a sensory task, aiming to find samples with spatially distributed abnormal pixels within the same category (Rippel, Mertens, and Merhof 2021; Jiang et al. 2022). It requires a finer granularity and better discrimination of positive and negative samples as the distribution of defects is often structured and localized. Patch SVDD (Yi and Yoon 2020) introduces the SVDD algorithm at the patch level and employs self-supervised learning to form multiple finer-grained centers, enhancing the model’s ability to detect and locate local anomalies. DSPSVDD (Zhang and Deng 2021) combines deep feature extraction with data structure information, designing an enhanced comprehensive optimization objective by simultaneously minimizing hypersphere volume and network reconstruction error. SE-SVDD (Hu, Chen, and Shao 2021) proposes a semantic-enhanced anomaly detection method based on Deep SVDD, enhancing feature representation through cosine similarity and estimating pixel-wise anomaly scores using a multi-level structure. While these methods enhance the model’s sensitivity to local anomalies and improve OCC performance on this task, existing OCC methods still significantly lag behind the SOTA methods. In comparison, our method achieves SOTA-level results on this task with fewer parameters.

## 3 Exploring the Optimization Objective for Anomaly Detection

In this section, we first reviewed the SVDD and Deep SVDD methods. Based on their mathematical definitions, we conducted a rigorous and comprehensive theoretical analysis and derivation of the optimization objective space in OCC, aiming to find the properties that the optimal optimization

objective space should possess. Finally, we designed a simple and effective OCC method.

### 3.1 Recall on SVDD and Deep SVDD

We consider the anomaly detection task where the training set  $\mathbf{x} \in \mathcal{X}_{train}$  contains only normal samples, and anomaly samples are only available during the testing phase. Following the notation and theoretical analysis of SVDD, all normal samples need to align with the hypersphere center  $\mathbf{c}$  of the OCC optimization objective. The process is defined as:

$$F(R, \mathbf{c}) = R^2 \quad (1)$$

With the constraints:

$$\|\mathbf{x}_i - \mathbf{c}\|^2 \leq R^2, \forall \mathbf{x}_i \in \mathcal{X}_{train} \quad (2)$$

$R$  is the radius of the sphere. Incorporating Lagrangian, Eq.2 can be rewrote:

$$L(R, \mathbf{c}, \alpha_i) = R^2 - \sum_i \alpha_i \{R^2 - \|\mathbf{x}_i - \mathbf{c}\|^2\} \quad (3)$$

$\alpha$  is the Lagrange multipliers. By setting the gradients of the relevant parameters to zero, Eq.3 needs to satisfy the following constraints:

$$\frac{\partial L}{\partial R} = 0 \rightarrow \sum_i \alpha_i = 1 \quad (4)$$

$$\frac{\partial L}{\partial \mathbf{c}} = 0 \rightarrow \mathbf{c} = \sum_i \alpha_i \mathbf{x}_i \quad (5)$$

As a result, the hypersphere center  $\mathbf{c}$  of SVDD can be represented as a linear combination of training samples. Subsequent works such as Deep SVDD extend Eq.5 and represent the hypersphere center  $\mathbf{c}$  as the average of pre-trained features. In addition to this, Deep SVDD empirically analyzes that improper settings of neural networks can lead to the pattern collapse issue, including all weights of the neural network being zero, inappropriate biases and activation functions. Although Deep SVDD provides valuable guidance, rigorous mathematical analysis is still lacking.

### 3.2 Theory Analysis for Optimization Objective

Previous methods have focused primarily on the design of the network structure, typically by empirically setting the hypersphere center  $\mathbf{c}$  to the average of the pre-trained features. However, as the optimization objective of the entire network,  $\mathbf{c}$  is also a potential crucial factor influencing performance. In this section, we will thoroughly explore  $\mathbf{c}$ .

**Optimization Objective can be data-agnostic.** Assuming the neural network  $\varphi(\cdot)$  is with learnable parameters  $W$ , Eq.3 is modified as follows:

$$\begin{aligned} L(R, \mathbf{c}, \alpha_i, W) &= R^2 - \sum_i \alpha_i \{R^2 - \|\varphi(\mathbf{x}_i, W) - \mathbf{c}\|^2\} \\ &= R^2 - \sum_i \alpha_i R^2 + \sum_i \alpha_i \|\varphi(\mathbf{x}_i, W) - \mathbf{c}\|^2 \end{aligned} \quad (6)$$

By setting the gradients of relevant parameters to zero, the constraint in Eq.6 needs to be satisfied:

$$\frac{\partial L}{\partial R} = 2R - \sum_i 2\alpha_i R = 0 \rightarrow \sum_i \alpha_i = 1 \quad (7)$$

$$\begin{aligned} \frac{\partial L}{\partial W} &= 2 \sum_i \alpha_i W [\varphi(\mathbf{x}_i, W) - \mathbf{c}] = 0 \\ &\rightarrow \sum_i \alpha_i \varphi(\mathbf{x}_i, W) = \mathbf{c}, \text{ or } W = 0 \end{aligned} \quad (8)$$

According to Eq.8, two situations may occur when the objective function  $L$  stops optimization:

**Case 1:** When all the learnable weights of the neural network  $\varphi(\cdot)$  are zero,  $W = 0$ . In this case, the network maps all samples to a single point, resulting in a degenerate solution. This is also pointed out as an inappropriate situation by Deep SVDD. If the neural network  $\varphi(\cdot)$  does not have constant parameters, the center  $\mathbf{c}$  in the optimization becomes a zero constant feature vector. Therefore, we can avoid this situation by limiting  $\varphi(\cdot)$  to have only trainable parameters and setting  $\mathbf{c}$  as a non-zero constant feature vector.

**Case 2:** For any input sample,  $\sum_i \alpha_i \varphi(\mathbf{x}_i) = \mathbf{c}$ . If we fix the hypersphere center  $\mathbf{c}$ , the neural network, leveraging its powerful non-linear mapping ability, will automatically adjust the learnable parameters  $W$  to weight the distribution of the original feature space and map it to the target space. This means that the optimization objective  $\mathbf{c}$  is decoupled from the data, and can be set arbitrarily without considering the underlying data distribution assumption. This conclusion holds even when generalized to more complex neural networks, as they offer a more powerful non-linear fitting capability to ensure the convergence of the mapping to  $\mathbf{c}$ . In this study, we attempted to set  $\mathbf{c}$  sampled from standard normal distribution, uniform distribution, all-one distribution, and the average of sample pre-trained features. We observed that the model's anomaly detection performance did not exhibit any degree of deterioration, validating our viewpoint.

However, one necessary condition among these is that all normal features can be mapped to this optimization objective space  $\mathbf{c}$ . If the value of  $\mathbf{c}$  is set improperly, the normal sample space might not be able to map to the target space, resulting in the model's inability to capture all normal patterns and thus a decrease in accuracy. Meanwhile, the network tends to fit those minority outlier points, leading to pattern collapse. The optimization objective space  $\mathbf{c}$  should be a subset of the collection of mapped feature spaces. Therefore, as long as the norm of  $\mathbf{c}$  is reasonably set, the type or distribution of the target space  $\mathbf{c}$  can be arbitrary and data-independent.

**What is the Suitable Norm?** When the model approaches convergence, it can be approximated that Eq.7 and Eq.8 hold true. Substituting Eq.7 into Eq.6, we obtain:

$$L(\mathbf{c}, \alpha_i, W) = \sum_i \alpha_i \varphi(\mathbf{x}_i, W)^2 - 2 \sum_i \alpha_i \varphi(\mathbf{x}_i, W) \mathbf{c} + \mathbf{c}^2 \quad (9)$$

With Eq.8, the above Eq.9 can be simplified:

$$\begin{aligned} L(\alpha_i, W) &= \sum_i \alpha_i \varphi(\mathbf{x}_i, W)^2 - \left[ \sum_i \alpha_i \varphi(\mathbf{x}_i, W) \right]^2 \\ &= \sum_i \alpha_i (\varphi(\mathbf{x}_i, W), \varphi(\mathbf{x}_i, W)) \\ &\quad - \sum_{i,j} \alpha_i \alpha_j (\varphi(\mathbf{x}_i, W), \varphi(\mathbf{x}_j, W)) \end{aligned} \quad (10)$$

Let  $\mathbf{z}_i = \varphi(\mathbf{x}_i, W)$ , continuing the simplification:

$$\begin{aligned} L(\alpha_i, \mathbf{z}_i) &= \sum_i \alpha_i (\mathbf{z}_i, \mathbf{z}_i) - \sum_{i,j} \alpha_i \alpha_j (\mathbf{z}_i, \mathbf{z}_j) \\ &= \sum_i \alpha_i \|\mathbf{z}_i\|^2 - \sum_{i,j} \alpha_i \alpha_j \|\mathbf{z}_i\| \cdot \|\mathbf{z}_j\| \cdot \cos \theta_{ij} \end{aligned} \quad (11)$$

For a training set composed solely of normal samples, we can make the assumption that the norm difference of  $\forall i, j, \mathbf{z}_i, \mathbf{z}_j$  is not significant, and we can approximate it as  $\|\mathbf{z}_i\| \approx r, \|\mathbf{z}_j\| \approx r, \cos \theta_{ij} \approx 1, \sin \theta_{ij} \approx 0$ , thus:

$$L(r, \theta, \alpha_i) \approx \sum_i \alpha_i r^2 - \sum_{i,j} \alpha_i \alpha_j r^2 \cos \theta_{ij} \quad (12)$$

Taking the derivative of  $L$  and continuing to optimize the model until it fully converges:

$$\frac{\partial L}{\partial r} \approx 2r \left( \sum_i \alpha_i - \sum_{i,j} \alpha_i \alpha_j \right) \quad (13)$$

$$\frac{\partial L}{\partial \theta} \approx \sum_{i,j} \alpha_i \alpha_j r^2 \sin \theta_{ij} \quad (14)$$

With Eq.13 and  $\sin \theta_{ij} \approx 0$ , the gradient of feature norm  $r$  is greater than the  $\theta$  direction, thus the convergence speed is faster along  $r$ . Assuming that the optimization along the  $r$  direction is mostly complete at this point, then  $r$  is approximately equal to the norm of  $c$ . We can discuss Eq.14 as follows:

If the norm of the OCC optimization objective  $c$  is set to be too large,  $r$  will also be large. To continue optimizing  $L$  along the direction, the model must rapidly decrease the angle between  $\mathbf{z}_i$  and  $\mathbf{z}_j, \forall i, j$ , to achieve convergence in the  $\theta_{ij}$  direction. This is harmful because the model rapidly loses sensitivity to the angles of the samples, especially when abnormal samples similar to normal samples are input into the model (as their angle with normal samples is small). The experimental results in Section 5.3 confirm this point: as the norm of the OCC optimization objective  $c$  increases, the cosine similarity between the abnormal and normal samples increases rapidly, accompanied by a significant decrease in detection performance. Thus the norm of OCC optimization objective is the critical factor affecting performance.

**Our Assertions.** Based on the above theoretical analysis, we assert that the optimization objective of OCC can be arbitrarily set as long as it adheres to the following constraints:

**Assertion 1:** The hypersphere center  $c$  can be any hypersphere with a suitable norm and should not be large, without the need for prior knowledge about the training dataset. However, obviously degenerate case like  $c = 0$ , which

would lead to trivial solutions by simply setting all network parameters to zero, is excluded.

**Assertion 2:** While we observe that larger norm values tend to lead to decreased performance, the acceptable norm range varies based on different application scenarios due to differing cosine similarities between positive and negative samples. Overall, norm values and cosine similarity appear to have an inverse relationship. For instance, in tasks like OCC on CIFAR-10 (Krizhevsky, Hinton et al. 2009), which focus on semantic deviations, positive and negative samples belong to different categories and have lower similarity, allowing for a larger acceptable norm range. Conversely, in tasks like anomaly detection and segmentation on MVTEC AD (Bergmann et al. 2019), which emphasize perceptual deviations, positive and negative samples belong to the same category and exhibit higher similarities, leading to a smaller acceptable norm range.

**Assertion 3:** For uniformity, we advocate using random vectors sampled from the standard normal distribution as hypersphere centers, with their L2 norms kept at 1. This setting has demonstrated superiority across multiple datasets.

**Declaration of Advantages.** These findings form the basis for OCC methods to smoothly shift towards online anomaly detection, enabling cold startups without prior training data. Informed by this theory, the devised method can operate independently of distribution assumptions, exhibit model-agnosticism, and remain data-agnostic. A simple implementation is detailed in Section 3.3.

### 3.3 A Simple Implementation of Network

**Initialization Phase.** As illustrated in Fig.1, the network consists of an encoder pre-trained on the ImageNet dataset and a trainable projector. We follow the standard and common settings, consistent with previous methods: for image one-class classification tasks, the penultimate layer of features from the pre-trained backbone is used. For image anomaly detection and segmentation tasks, multi-scale features are aggregated. The projector is used to map pre-trained features into the hypersphere space centered around  $c$ . The projector is set as a  $1 \times 1$  convolutional layer by default. Despite simple, it demonstrates good detection performance. The hypersphere center  $c$  is randomly sampled from the standard normal distribution and normalized.

**Training Phase.** During training, the model first extracts and concatenates the pre-trained feature,  $\mathbf{f}_i = E(\mathbf{x}_i)$ , from normal samples, followed by projecting  $\mathbf{f}_i$  to the hypersphere:  $\mathbf{z}_i = \mathcal{P}(\mathbf{f}_i)$ . The loss function is defined using the Euclidean L2 distance to map the pre-trained feature  $\mathbf{f}_i$  of normal samples into the hypersphere centered around  $c$ :

$$L_W = \max(\|\mathbf{z}_i - c\|^2 - R^2, 0) \quad (15)$$

**Testing Phase.** In the testing phase, for a test sample  $\mathbf{x} \in \mathcal{X}_{test}$ , we compute the pre-trained feature  $\mathbf{f}_{test} = E(\mathbf{x}_{test})$  and the feature after projection  $\mathbf{z}_{test} = \mathcal{P}(\mathbf{f}_{test})$ . The decision function for anomaly detection is defined as:

$$\mathcal{D}(\mathbf{z}_{test}) = 1\{d > R\} \quad (16)$$

where  $d = \|\mathbf{z}_{test} - c\|$  is the L2 distance between  $\mathbf{z}_{test}$  and the OCC optimization objective  $c$ . Additionally, for image

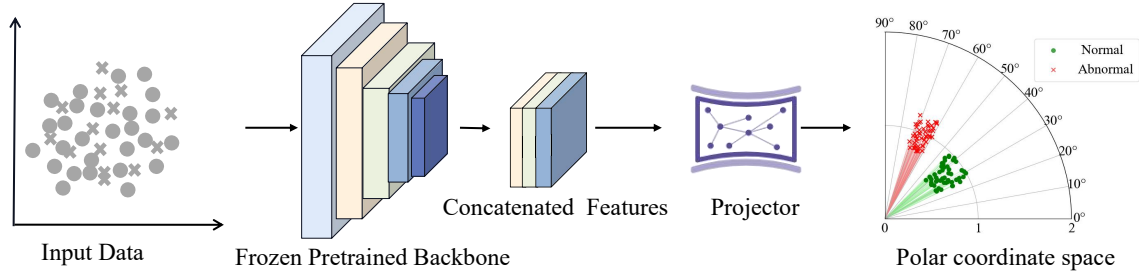


Figure 1: A simple implementation of our method for image anomaly detection and segmentation tasks. We use multi-scale concatenated features, as done in previous methods. As for OCC tasks, the only difference is that we use the penultimate layer of features of the pre-trained backbone. Our method gains excellent performance in polar coordinate space for distinguishing positive and negative samples by setting the optimization objective with suitable norms.

anomaly segmentation tasks, the abnormal scores are computed based on the L2 distance to the hypersphere center:

$$S = \max(\|z_i - c\|^2 - R^2, 0) \quad (17)$$

The pseudo-codes of our method are provided in Supplementary Material.

## 4 Evaluation of Methods

In this section, comprehensive evaluations are conducted to obtain the performance of our method among different tasks: (1) image one-class classification task (Section 4.2); (2) industrial image anomaly detection and segmentation task (Section 4.3); (3) online industrial image anomaly detection and segmentation task (Section 4.4). More details can be found in the Supplementary Material.

### 4.1 Implementation Details

**Evaluation Protocols, Datasets and Metrics.** Our method follows two standard and one self-defined protocols for evaluation. The images in the training and inference phases are first resized to  $256 \times 256$ , then center-cropped to  $224 \times 224$ , and finally fed into the network after normalization. Any additional transformations are not used. Our code was run on a single NVIDIA 3090 GPU with pytorch 1.10.

**Protocol A: I-OCC Task.** The anomaly detection performance on the image one-class classification task (I-OCC) are evaluated with five common standard datasets: Fashion MNIST (Xiao, Rasul, and Vollgraf 2017), CIFAR10 (Krizhevsky, Hinton et al. 2009), CIFAR100 (Krizhevsky, Hinton et al. 2009), CatsVsDogs (Elson et al. 2007) and MVTec AD (Bergmann et al. 2019). Except for MVTec AD, the other datasets select one category as normal and all the remaining categories as anomalies. The MVTec AD dataset contains normal data and explicit anomalies in the same category. We evaluate the image-level average ROC AUC % and the model trainable parameter size.

**Protocol B: I-ADS Task.** We evaluate methods on the more fine-grained industrial image anomaly detection and segmentation task (I-ADS). Following the standard protocol,

the image-level average ROC AUC % and the pixel-level average ROC AUC % are evaluated. Besides MVTec AD, two common standard industrial image datasets, MPDD (Jezek et al. 2021) and VisA (Zou et al. 2022), are also used.

**Protocol C: Online Anomaly Detection.** Our method is evaluated on online industrial image anomaly detection and segmentation task to validate its excellent scalability for online detection, where the batch size is set to 1 for simulating streaming data with MVTec AD, MPDD and VisA datasets. The image-level ROC AUC % and the pixel-level average ROC AUC % are evaluated.

**Methods of Comparison.** We compared our method to the SOTA methods separately under each protocol. This is due to the fact that many SOTA methods in Protocol A have not been evaluated in the I-ADS task of Protocol B, or they are significantly far behind the SOTA. For Protocol A, we compare with the SOTA methods including Deep SVDD (Ruff et al. 2018), PANDA (Reiss et al. 2021), MS (Reiss and Hoshen 2023), MRot (Hendrycks et al. 2019), and IGD (Chen et al. 2022). For Protocol B, we compare with Patch SVDD (Yi and Yoon 2020), PaDiM (Defard et al. 2021), DRAEM (Zavrtanik, Kristan, and Skočaj 2021), FastFlow (Yu et al. 2021), STPM (Zolfaghari and Sajedi 2022) and CFA (Lee, Lee, and Song 2022). If the original results of these SOTA methods are available, we use them directly, otherwise we perform our own evaluation (if possible). Notably, if other methods reported performance for more than one variant, we defaulted to comparing with the best variant.

### 4.2 Protocol A: Evaluation on Image One-Class Classification Task

As depicted in Table 1, our method demonstrates performance on par with, if not surpassing, the current state-of-the-art methods across multiple datasets. Notably, on the MVTec AD dataset, our method achieves a substantial performance gain, surpassing the second-ranked IGD by 5.6%. It is imperative to highlight that the trainable parameters within our method are minimal among pre-trained-based methods. Our approach is free to select any data-agnostic feature space, thereby obviating the need for pre-collecting datasets. Given

Methods	DSVDD	PANDA	MS	IGD	MRot	Ours
FMNIST	84.8	<b>95.6</b>	-	94.4	93.2	<b>95.4</b>
CIFAR10	64.8	<b>96.2</b>	<b>97.2</b>	91.3	90.1	93.9
CIFAR100	67.0	94.1	<b>96.4</b>	84.3	80.1	<b>96.5</b>
CatsVSDogs	50.5	97.3	<b>99.3</b>	-	86.0	<b>97.5</b>
MVTec AD	77.9	86.5	87.2	<b>93.4</b>	65.5	<b>99.0</b>
Train Params [MB]	<b>1.3</b>	55.6	55.6	28.7	11.3	<b>3.7</b>

Table 1: Protocol A: One-Class Classification Performance (Average Image ROC AUC %). Bold is the SOTA performance and second ranks. Our method achieves SOTA performance with fewer trainable parameters.

Metric	Average Image ROC AUC %			Average Pixel ROC AUC %		
	MVTec AD	MPDD	VisA	MVTec AD	MPDD	VisA
IGD	93.4	83.1	84.7	93.1	86.8	85.4
CFA	98.1	92.3	92.0	97.1	94.8	84.3
PaDiM	90.8	70.6	89.1	96.6	95.5	98.1
DRAEM	98.1	<b>94.1</b>	88.7	97.5	91.8	93.5
FastFlow	90.5	88.7	87.4	95.5	80.8	91.1
STPM	92.4	87.6	83.3	95.4	98.1	83.4
PatchSVDD	92.1	86.3	-	95.7	81.4	-
Ours	<b>99.0</b>	92.3	<b>93.7</b>	<b>98.2</b>	<b>98.2</b>	<b>98.2</b>

Table 2: Protocol B: Industrial Image Anomaly Detection and Segmentation Performance. Our method outperforms in MVTEC AD, MPDD and VisA datasets.

the practical constraints wherein datasets often emerge in an incomplete state at the initial stage, this highlights the flexibility, generality, and practicality of our method.

### 4.3 Protocol B: Evaluation on Industrial Image Anomaly Detection and Segmentation

In the fine-grained industrial image anomaly detection and segmentation task, we conduct comprehensive comparisons with a multitude of state-of-the-art (SOTA) methods. Moreover, the top-performing OCC method IGD from Protocol A is also benchmarked. As depicted in the Table 2, our method is SOTA on both the image-level average ROC AUC % and the pixel-level average ROC AUC %. Notably, while other methods might exhibit high accuracy in a single task (I-OCC/I-ADS), our method achieves SOTA performance in both tasks without requiring elaborate adjustments. In other word, it is proficient in handling both OCC tasks that emphasize semantic deviations and anomaly detection and segmentation tasks that focus on finer-grained statistical deviations. This can be attributed to the remarkably flexible, generic, and data-agnostic optimization objective of our method.

### 4.4 Protocol C: Expansion to Online Anomaly Detection Task

As shown in the Table 3, our approach’s online detection performance on the MVTEC AD, MPDD and VisA datasets is on par with some SOTA methods from Table 2. This performance is remarkably surprising, as it is an unfair comparison for our method: while other methods can repeatedly use pre-collected training samples, ours can only leverage samples in a one-pass manner. This solidly confirms one of the key conclusions of this study: by considering any space

Metric	MVTec AD	MPDD	VisA
Average Image ROC AUC %	93.4	84.5	93.0
Average Pixel ROC AUC %	95.6	97.2	98.1

Table 3: Protocol C: Online Image Anomaly Detection and Segmentation Performance. Our method even outperforms some offline learning SOTA methods in Protocol B.

with an appropriate norm as the optimization objective for OCC methods, we address the data-agnostic requirement of model initialization in online anomaly detection, eliminating the pre-collection of data. Thus, our method provides a flexible, general, and effective foundation for pushing current offline learning OCC methods towards the online paradigm.

## 5 Ablations

Thorough ablation experiments and visualization analyses are implemented to evaluate the following topics: (1) visual analysis (Section 5.1) to validate the conclusions of Section 3.2 ; (2) the impact of distribution type (Section 5.2); (3) the norm of the optimization objective and guidelines for feasible domain of norm (Section 5.3). More ablations can be found in Supplementary Material.

### 5.1 Visualization

**Norm-based Degradation of OCC methods.** By visualizing in Fig. 2, we examine the positive and negative sample discriminatory power of the OCC method with the optimization objective set to different norms. Observe Fig. 2, the conclusion of our theoretical analysis in Section 3.2 is proved: when the norm of the OCC optimization objective is too large, the neural network gradually loses its angular sensitivity to positive and negative samples, which finally degrades the detection performance.

### 5.2 Impact of Distribution Type

The distribution types of hypersphere centers are first analyzed in Table 4. When the norm of hypersphere centers is strictly limited to 1, the detection accuracy rarely decreases, regardless of whether the hypersphere centers come from pre-trained features or from random distributions. This validates assertion 1 in Section 3.2: when the norms are strictly consistent, the optimization objective of the OCC method can be set to data-agnostic any space, and the average of the pre-trained features commonly used by the previous method is just one of the solutions.

### 5.3 Impact of Norm of Hypersphere Center

**Impact of the norm of the OCC optimization objective.** As depicted in Fig. 3, with the hypersphere center’s norm increases, the detection performance on different datasets show a similar decreasing trend. This observation suggests that the optimization objective’s norm of the OCC method has a notable impact on the detection performance. Too large norms would weaken the ability of the OCC method to discriminate between positive and negative samples. But the different datasets have varying sensitivity thresholds.

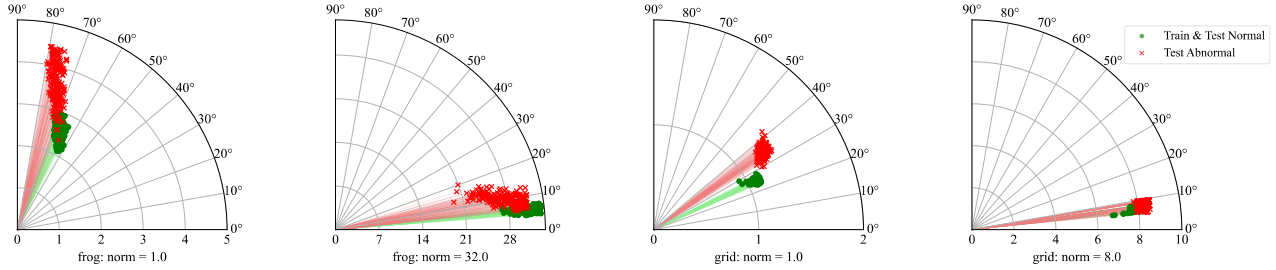


Figure 2: Illustration of the model’s positive and negative sample discrimination performance for the **frog** category in CIFAR10 and the **grid** category in the MVTeC AD dataset. Visualizing norm-based and angular discrimination. With the norm value increases, OCC model gradually diminishes sensitivity to angular differences between positive and negative samples. For instance, in the grid category, the angle between negative and positive samples decreases significantly at norm 8 compared to norm 1, implying increased challenge in sample discrimination.

Distribution Type	L2 Normalization	CIFAR10	MVTeC AD
Pre. Features	✓	93.88	98.97
$\mathcal{N}(0, 1)$	✓	93.93	99.00
$\mathcal{U}(0, 1)$	✓	93.91	98.96
$\mathcal{J}(1)$	✓	93.86	98.93

Table 4: Impact of distribution type of hypersphere center on anomaly detection performance. Average Image ROC AUC % is reported. Distribution type includes pre-trained features average, standard normal distribution  $\mathcal{N}(0, 1)$ , uniform distribution  $\mathcal{U}(0, 1)$  and  $\mathcal{J}(1)$  with each element is 1.

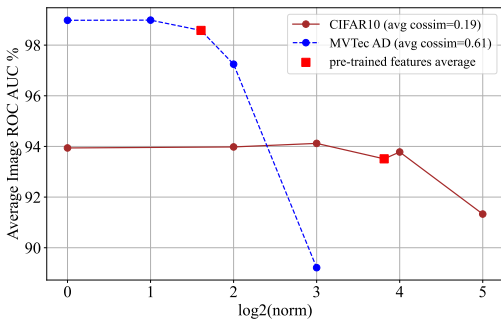


Figure 3: Impact of the OCC optimization objective’s norm.

**Guidelines for determining the feasible domain of the optimization objective.** As shown in Fig. 3, we observe that the performance degradation is significantly different across datasets: the method is more robust to norm changes of the hypersphere center on the CIFAR10 dataset, while it exhibits more sensitivity on the MVTeC AD dataset. We attribute this phenomenon to the semantic similarity between the positive and negative categories of the dataset. This validates our assertion 2 in Section 3.2: datasets with higher similarity between positive and negative samples entail a narrower feasible domain for the optimization objective’s norm of OCC.

To determine the feasible domain of the OCC optimization objective norm on different datasets, we have established empirical guiding principles based on experimental

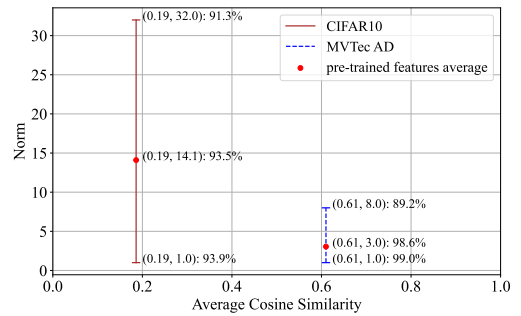


Figure 4: Feasible domains of the optimization objective’s norm. Average cosine similarity between positive and negative samples, norm value, average image ROC AUC % are reported.

results. As shown in Fig. 4, the pre-trained backbone is used to extract image features, and then the average cosine similarity of the pre-trained features for positive and negative samples is calculated (0.19 for CIFAR10 and 0.61 for MVTeC AD). When striving for an OCC method detection accuracy surpassing 90.0%, the feasible domain for the optimization objective’s norm is identified as [1,32] for CIFAR10 and [1,8) for MVTeC AD datasets. Significantly, it is noteworthy that the optimization objective configuration strategy employed by previous OCC methods (i.e., the average of pre-trained features) constitutes a solution within the feasible domains that we have given. Readers are encouraged to calculate the average cosine similarity for their own datasets, subsequently opting for an appropriate norm for the optimization objective of OCC based on the insights derived from the test results illustrated in Fig. 4.

## 6 Conclusion

In this study, we conducted a rigorous investigation into the optimization objective of one-class classification (OCC) and unveiled its interpretation in polar coordinates. The key to distinguishing positive and negative samples lies in the careful selection of the radius (norm) value, ensuring the model’s

sensitivity and discriminability among angular. We established the guidelines for determining feasible norm ranges of OCC optimization objectives. Furthermore, these insights paved the way for a simple, data-agnostic deep one-class classification method, facilitating OCC's transition towards online anomaly detection. Extensive experiments confirm the effectiveness of our theory and model, resulting in state-of-the-art performance across OCC tasks and industrial image anomaly detection and segmentation.

**Limitations.** However, it's important to note that our method considers cases with entirely normal training sets and does not address potential anomalies, particularly relevant in online scenarios. Our initial exploration into online anomaly detection offers room for further enhancements. Future work will refine our theory and model to achieve complete online anomaly detection capabilities.

## References

- Bergmann, P.; Fauser, M.; Sattlegger, D.; and Steger, C. 2019. MVTEC AD-A comprehensive real-world dataset for unsupervised anomaly detection. In *Proceedings of the IEEE/CVF conference on computer vision and pattern recognition*, 9592–9600.
- Chen, Y.; Tian, Y.; Pang, G.; and Carneiro, G. 2022. Deep one-class classification via interpolated gaussian descriptor. In *Proceedings of the AAAI Conference on Artificial Intelligence*, 383–392.
- Defard, T.; Setkov, A.; Loesch, A.; and Audigier, R. 2021. Padim: a patch distribution modeling framework for anomaly detection and localization. In *Pattern Recognition. ICPR International Workshops and Challenges: Virtual Event, January 10–15, 2021, Proceedings, Part IV*, 475–489. Springer.
- Deng, J.; Dong, W.; Socher, R.; Li, L.-J.; Li, K.; and Fei-Fei, L. 2009. Imagenet: A large-scale hierarchical image database. In *2009 IEEE conference on computer vision and pattern recognition*, 248–255. Ieee.
- Elson, J.; Douceur, J. R.; Howell, J.; and Saul, J. 2007. Asirra: a CAPTCHA that exploits interest-aligned manual image categorization. *CCS*, 7: 366–374.
- Gudovskiy, D.; Ishizaka, S.; and Kozuka, K. 2022. Cflowad: Real-time unsupervised anomaly detection with localization via conditional normalizing flows. In *Proceedings of the IEEE/CVF Winter Conference on Applications of Computer Vision*, 98–107.
- Hendrycks, D.; Mazeika, M.; Kadavath, S.; and Song, D. 2019. Using self-supervised learning can improve model robustness and uncertainty. *Advances in neural information processing systems*, 32.
- Hu, C.; Chen, K.; and Shao, H. 2021. A semantic-enhanced method based on deep SVDD for pixel-wise anomaly detection. In *2021 IEEE International Conference on Multimedia and Expo (ICME)*, 1–6. IEEE.
- Jang, J.; Hwang, E.; and Park, S.-H. 2023. N-pad: Neighboring pixel-based industrial anomaly detection. In *Proceedings of the IEEE/CVF Conference on Computer Vision and Pattern Recognition*, 4364–4373.
- Jezeq, S.; Jonak, M.; Burget, R.; Dvorak, P.; and Skotak, M. 2021. Deep learning-based defect detection of metal parts: evaluating current methods in complex conditions. In *2021 13th International Congress on Ultra Modern Telecommunications and Control Systems and Workshops (ICUMT)*, 66–71. IEEE.
- Jiang, X.; Liu, J.; Wang, J.; Nie, Q.; Wu, K.; Liu, Y.; Wang, C.; and Zheng, F. 2022. Softpatch: Unsupervised anomaly detection with noisy data. *Advances in Neural Information Processing Systems*, 35: 15433–15445.
- Krizhevsky, A.; Hinton, G.; et al. 2009. Learning multiple layers of features from tiny images. <https://www.cs.toronto.edu/~kriz/cifar.html>. Accessed: 2009.
- Lee, S.; Lee, S.; and Song, B. C. 2022. Cfa: Coupled-hypersphere-based feature adaptation for target-oriented anomaly localization. *IEEE Access*, 10: 78446–78454.
- Nguyen, A.; Yosinski, J.; and Clune, J. 2015. Deep neural networks are easily fooled: High confidence predictions for unrecognizable images. In *Proceedings of the IEEE conference on computer vision and pattern recognition*, 427–436.
- Reiss, T.; Cohen, N.; Bergman, L.; and Hoshen, Y. 2021. Panda: Adapting pretrained features for anomaly detection and segmentation. In *Proceedings of the IEEE/CVF Conference on Computer Vision and Pattern Recognition*, 2806–2814.
- Reiss, T.; and Hoshen, Y. 2023. Mean-shifted contrastive loss for anomaly detection. In *Proceedings of the AAAI Conference on Artificial Intelligence*, 2155–2162.
- Rippel, O.; Mertens, P.; and Merhof, D. 2021. Modeling the distribution of normal data in pre-trained deep features for anomaly detection. In *2020 25th International Conference on Pattern Recognition (ICPR)*, 6726–6733. IEEE.
- Roth, K.; Pemula, L.; Zepeda, J.; Schölkopf, B.; Brox, T.; and Gehler, P. 2022. Towards total recall in industrial anomaly detection. In *Proceedings of the IEEE/CVF Conference on Computer Vision and Pattern Recognition*, 14318–14328.
- Ruff, L.; Vandermeulen, R.; Goernitz, N.; Deecke, L.; Siddiqui, S. A.; Binder, A.; Müller, E.; and Kloft, M. 2018. Deep one-class classification. In *International conference on machine learning*, 4393–4402. PMLR.
- Schölkopf, B.; Williamson, R. C.; Smola, A.; Shawe-Taylor, J.; and Platt, J. 1999. Support vector method for novelty detection. *Advances in neural information processing systems*, 12.
- Tax, D. M.; and Duin, R. P. 2004. Support vector data description. *Machine learning*, 54: 45–66.
- Xiao, H.; Rasul, K.; and Vollgraf, R. 2017. Fashion-mnist: a novel image dataset for benchmarking machine learning algorithms. arXiv:1708.07747.
- Yang, M.; Wu, P.; and Feng, H. 2023. MemSeg: A semi-supervised method for image surface defect detection using differences and commonalities. *Engineering Applications of Artificial Intelligence*, 119: 105835.
- Yi, J.; and Yoon, S. 2020. Patch svdd: Patch-level svdd for anomaly detection and segmentation. In *Proceedings of the Asian Conference on Computer Vision*.



Yu, J.; Zheng, Y.; Wang, X.; Li, W.; Wu, Y.; Zhao, R.; and Wu, L. 2021. Fastflow: Unsupervised anomaly detection and localization via 2d normalizing flows. arXiv:2111.07677.

Zavrtanik, V.; Kristan, M.; and Skočaj, D. 2021. Draem-a discriminatively trained reconstruction embedding for surface anomaly detection. In *Proceedings of the IEEE/CVF International Conference on Computer Vision*, 8330–8339.

Zhang, Z.; and Deng, X. 2021. Anomaly detection using improved deep SVDD model with data structure preservation. *Pattern Recognition Letters*, 148: 1–6.

Zolfaghari, M.; and Sajedi, H. 2022. Unsupervised Anomaly Detection with an Enhanced Teacher for Student-Teacher Feature Pyramid Matching. In *2022 27th International Computer Conference, Computer Society of Iran (CSICC)*, 1–4. IEEE.

Zou, Y.; Jeong, J.; Pemula, L.; Zhang, D.; and Dabeer, O. 2022. SPot-the-Difference Self-supervised Pre-training for Anomaly Detection and Segmentation. In *Computer Vision–ECCV 2022: 17th European Conference, Tel Aviv, Israel, October 23–27, 2022, Proceedings, Part XXX*, 392–408. Springer.

## Appendix

### A Datasets

In this paper, the OCC methods are evaluated on seven datasets, including Fashion MNIST, CIFAR10, CIFAR100, CatsVsDogs, MVTec AD, MPDD, and VisA. The category information is shown in Table S1 and some of the samples are shown in Fig. S1. For the Fashion MNIST, CIFAR10, CIFAR100, and CatsVsDog datasets, we selected one category as the normal category and the others as the abnormal categories. Meanwhile, for the MVTec AD, MPDD and VisA datasets, normal and abnormal samples belong to the same category.

### B Methods Details

#### B.1 Network Structure and Optimizer

Since we proved that the optimization objective of the OCC method can be set to arbitrary space with a suitable norm (in Section 3.2), in all evaluations, the hypersphere center is by default random sampled from the standard normal distribution  $\mathcal{N}(0, 1)$  with L2 normalization. The random seed is fixed to 1024. In **Protocol A**, the batch size is set to 64. We first use the penultimate layer of the pre-trained ResNet152 backbone on the ImageNet dataset as the embedded feature  $f$  (with dimension 2048). The projector is set by default to be a  $1 \times 1$  convolutional layer with a bias term, which maps the feature  $f$  into the latent feature  $z$ , keeping the feature dimension unchanged. The optimizer is set to Adam, with an initial learning rate of  $1e-4$  and a decay rate of  $5e-4$ . Training epochs are 20. In **Protocol B**, the batch sizes are set by default to 16, 8, and 8 for MVTec AD, MPDD, and VisA. The embedded features  $f \in \mathcal{R}^{B \times 1792 \times 56 \times 56}$ , consist of layers 2, 3, and 4 of the pre-trained Wider Resnet 50 backbone, which is a common and standard setup for industrial image anomaly detection and segmentation. The optimizer settings

Datasets	Category	Train	Test	Image Size (min/max)
FMNIST	10	60000	10000	28/28
CIFAR10	10	50000	10000	32/32
CIFAR100	100	50000	10000	32/32
CatsVsDogs	2	8750	7500	280/500
MVTec AD	15	4096	1258	512/512
MPDD	6	1064	282	1024/1024
VisA	12	10621	1200	960/1562

Table S1: Detailed information of datasets, including the number of categories, the total number of samples in the training and test sets, and the minimum/maximum image sizes.

are the same as in Protocol A. Training epochs are 50. In **Protocol C**, all settings are the same as in Protocol B, except that the batch size is 1 to simulate the online streaming data, where the sample is one-by-one input.

#### B.2 Pseudo Codes

We provide the pseudo-codes of our method for image one-class classification tasks (Protocol A) and industrial image anomaly detection and segmentation tasks (Protocol B), which are shown in Algorithm 1 and Algorithm 2.

Algorithm 1: Our Method for Image One-Class Classification Tasks.

- 
- 1: **Input:** ImageNet pre-trained encoder  $E$ , Projector  $\mathcal{P}$  (e.g.  $1 \times 1$  conv), Radius of hypersphere  $R = 1e^{-5}$ .
  - 2: **Training Stage:**
  - 3: Initialization:  $c \leftarrow$  standard normal distribution(0, 1)
  - 4: Train sample  $x_{\text{train}} \leftarrow$  normal samples
  - 5: Pre-trained feature  $f_{\text{train}} \leftarrow E(x_{\text{train}})$
  - 6: Mapped feature  $z_{\text{train}} \leftarrow \mathcal{P}(f_{\text{train}})$
  - 7:  $L_W \leftarrow \max(\|z_{\text{train}} - c\|^2 - R^2, 0)$
  - 8:  $L_W$ .backward()
  - 9: **Testing Stage:**
  - 10: Test sample  $x_{\text{test}} \leftarrow$  test dataset
  - 11: Pre-trained feature  $f_{\text{test}} \leftarrow E(x_{\text{test}})$
  - 12: Mapped feature  $z_{\text{test}} \leftarrow \mathcal{P}(f_{\text{test}})$
  - 13: Distance  $d \leftarrow \|z_{\text{test}} - c\|$
  - 14: **Output:** OCC detection decision  $\mathbf{1}\{d > R\}$
- 

## C Evaluation of Methods

### C.1 Accuracy

This section shows a detailed comparison of our methods and others for each category under standard protocols. We report the image-level average ROC AUC % in Table S4. Additionally, the visualization of detection results are shown in Fig. S2 and Fig. S3.

### C.2 Impact of Network Structure and Projector

We report the ablation of network structure and projector in Table S2 and Table S3. Obviously, our method can be well adapted to different backbones and projectors.

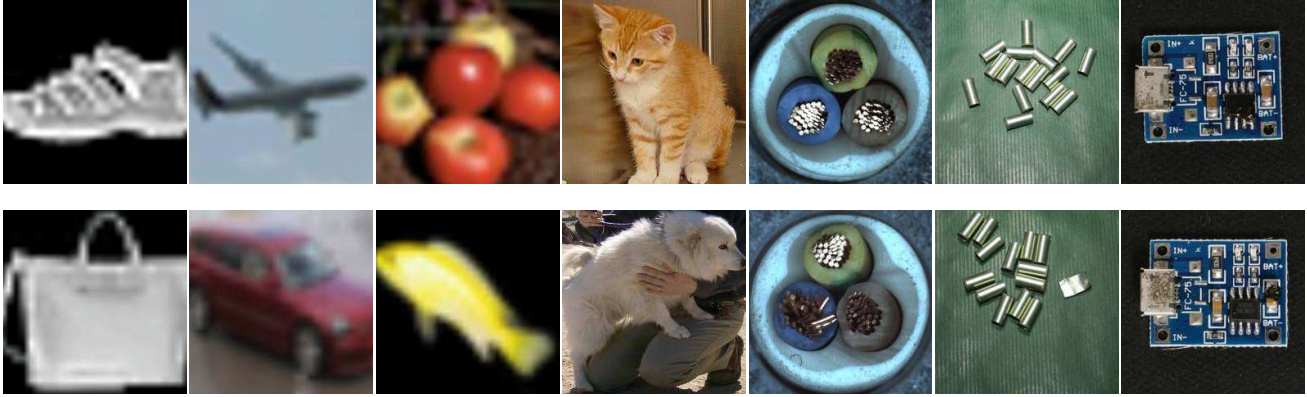


Figure S1: Samples of datasets. From left to right are Fashion MNIST, CIFAR10, CIFAR100, CatsVsDogs, MVTec AD, MPDD and VisA. The first row is the normal samples and the second row is the abnormal samples. Following the standard settings, for the Fashion MNIST, CIFAR10, CIFAR100, and CatsVsDogs datasets, we select any one category in the dataset as the normal category, e.g., airplanes in CIFAR10, and treat the other categories as the anomalous categories. For MVTec AD, MPDD and VisA, positive and negative samples are in the same category, e.g., bent wire type anomalies of cable category in MVTec AD dataset.

Backbones	CIFAR10	MVTec AD
Resnet18	88.6	78.49
Wider Resnet50	90.9	99.0
Resnet152	93.9	97.7

Table S2: Ablations of different backbones. The image-level average ROC AUC % is reported.

---

Algorithm 2: Our Method for Industrial Image Anomaly Detection and Segmentation Tasks.

---

- 1: **Input:** ImageNet pre-trained encoder  $E$ , Projector  $\mathcal{P}$  (e.g.  $1 \times 1$  conv), Radius of hypersphere  $R = 1e^{-5}$ .
  - 2: **Training Stage:**
  - 3: Initialization:  $c \leftarrow$  standard normal distribution(0, 1)
  - 4: Train sample  $x_{\text{train}} \leftarrow$  normal samples
  - 5: Multi-Scale Pre-trained feature  $\{f_{\text{train}}^{(i)}\}_{i=1}^3 \leftarrow E(x_{\text{train}})$
  - 6: Concated feature  $f_{\text{train}} \leftarrow$  Concated( $\{f_{\text{train}}^{(i)}\}_{i=1}^3$ )
  - 7: Mapped feature  $z_{\text{train}} \leftarrow P(f_{\text{train}})$
  - 8:  $L_W \leftarrow \max(\|z_{\text{train}} - c\|^2 - R^2, 0)$
  - 9:  $L_W$ .backward()
  - 10: **Testing Stage:**
  - 11: Test sample  $x_{\text{test}} \leftarrow$  test dataset
  - 12: Pre-trained feature  $f_{\text{test}} \leftarrow E(x_{\text{test}})$
  - 13: Mapped feature  $z_{\text{test}} \leftarrow P(f_{\text{test}})$
  - 14: **Output:** Anomaly Score  $\|z_{\text{test}} - c\|$
- 

Projectors	CIFAR10	MVTec AD
Conv1 $\times$ 1	93.9	99.0
Linear	93.9	97.3

Table S3: Ablations of different projectors. The image-level average ROC AUC % is reported.

## D Visualization

### D.1 Norm-based Degradation of OCC methods

We report in detailed the impact of the norm of the OCC optimization objective on the model’s ability to discriminate between positive and negative samples. Fig. S4 illustrates the frog category from CIFAR10 and the grid category from MVTec AD. As the norm of the OCC optimization objective increases, the model’s ability to distinguish between positive and negative samples on both categories shows a similar significant degradation.

### D.2 Impact of Norm of Hypersphere Center

Fig. S5, Table S5 and Table S6 show the impact of the different norms of the OCC optimization objective on each category. These results support the conclusions and results in Section 5.3: the feasible domain of the OCC optimization

Method	IGD	CFA	PaDiM	DRAEM	FastFlow	STPM	Patch SVDD	Ours
Bottle	100.0	100.0	99.4	96.9	91.2	100.0	96.9	100.0
Cable	85.9	99.4	85.0	93.4	99.2	74.8	89.5	98.4
Capsule	83.3	99.9	94.9	96.1	87.5	94.4	76.7	96.3
Carpet	80.0	94.7	88.9	96.3	88.1	92.5	95.7	99.9
Grid	60.0	99.7	90.4	100.0	98.8	77.4	89.9	99.6
Hazelnut	98.2	99.6	99.1	100.0	96.1	95.6	91.2	100.0
Leather	90.8	98.6	84.3	100.0	90.8	95.3	75.6	100.0
Metalnut	84.8	96.5	87.6	99.4	98.0	94.0	94.0	100.0
Pill	76.4	98.5	98.1	96.8	97.8	93.0	78.6	97.9
Screw	67.0	98.3	92.2	99.2	63.2	97.6	82.2	94.8
Tile	98.3	99.9	86.5	100.0	100.0	99.0	96.8	99.6
Toothbrush	90.8	100.0	100.0	99.7	88.1	100.0	98.9	100.0
Transformer	90.5	99.4	94.1	94.2	90.8	97.2	89.4	99.3
Wood	94.5	97.4	80.8	99.2	67.5	96.3	98.4	99.9
Zipper	90.5	88.8	80.9	99.7	100.0	78.5	98.0	99.2
<b>Avg</b>	86.3	98.1	90.8	98.1	90.5	92.4	90.1	99.0

Table S4: Industrial image anomaly detection and segmentation performance comparison on MVTEC AD. The image-level average ROC AUC % is reported.

Norms	1.0	4.0	8.0	16.0	32.0
Avg	93.9	94.0	94.1	93.8	91.3

Table S5: Detection performance under different norms of OCC optimization objective on CIFAR10. The image-level average ROC AUC % is reported.

Norms	1.0	2.0	4.0	8.0
Avg	99.0	99.0	97.2	89.2

Table S6: Detection performance under different norms of OCC optimization objective on MVTEC AD. The image-level average ROC AUC % is reported.

objective norm is closely related to the cosine similarity between positive and negative samples. The higher the cosine similarity, the smaller the feasible domain.

### D.3 Impact of Distribution Type of Hypersphere Center

We presents the t-SNE plot of the output features of the OCC model. As shown in Fig. S6, the output features of the OCC method exhibit similar properties despite the fact that the normalized optimization objective obeys different distributions, and the normal/abnormal discrimination performance is trivially affected.

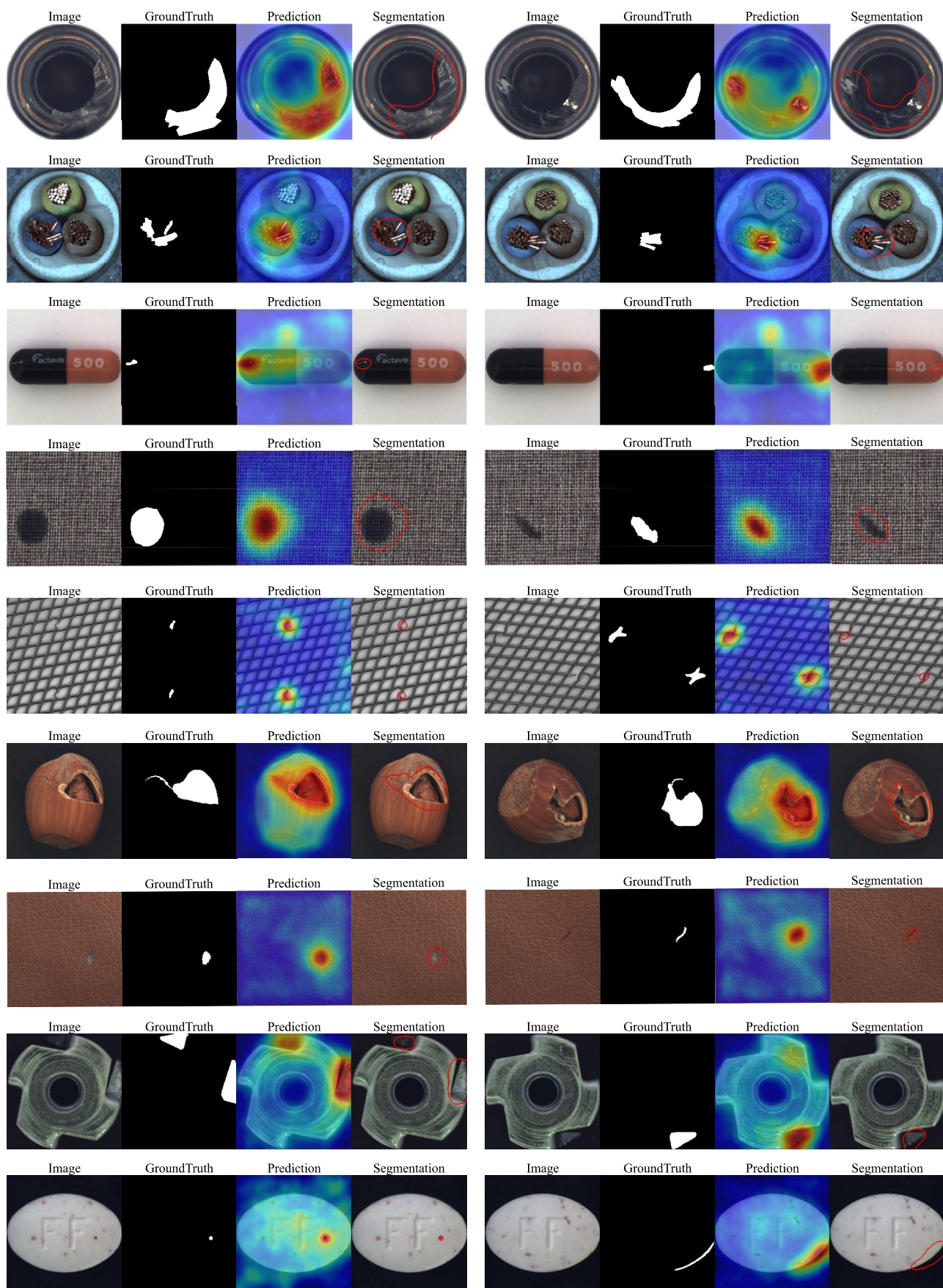


Figure S2: Visualization of 9 categories of MVTEC AD: bottle, cable, capsule, carpet, grid, hazelnut, leather, metal nut and pill.

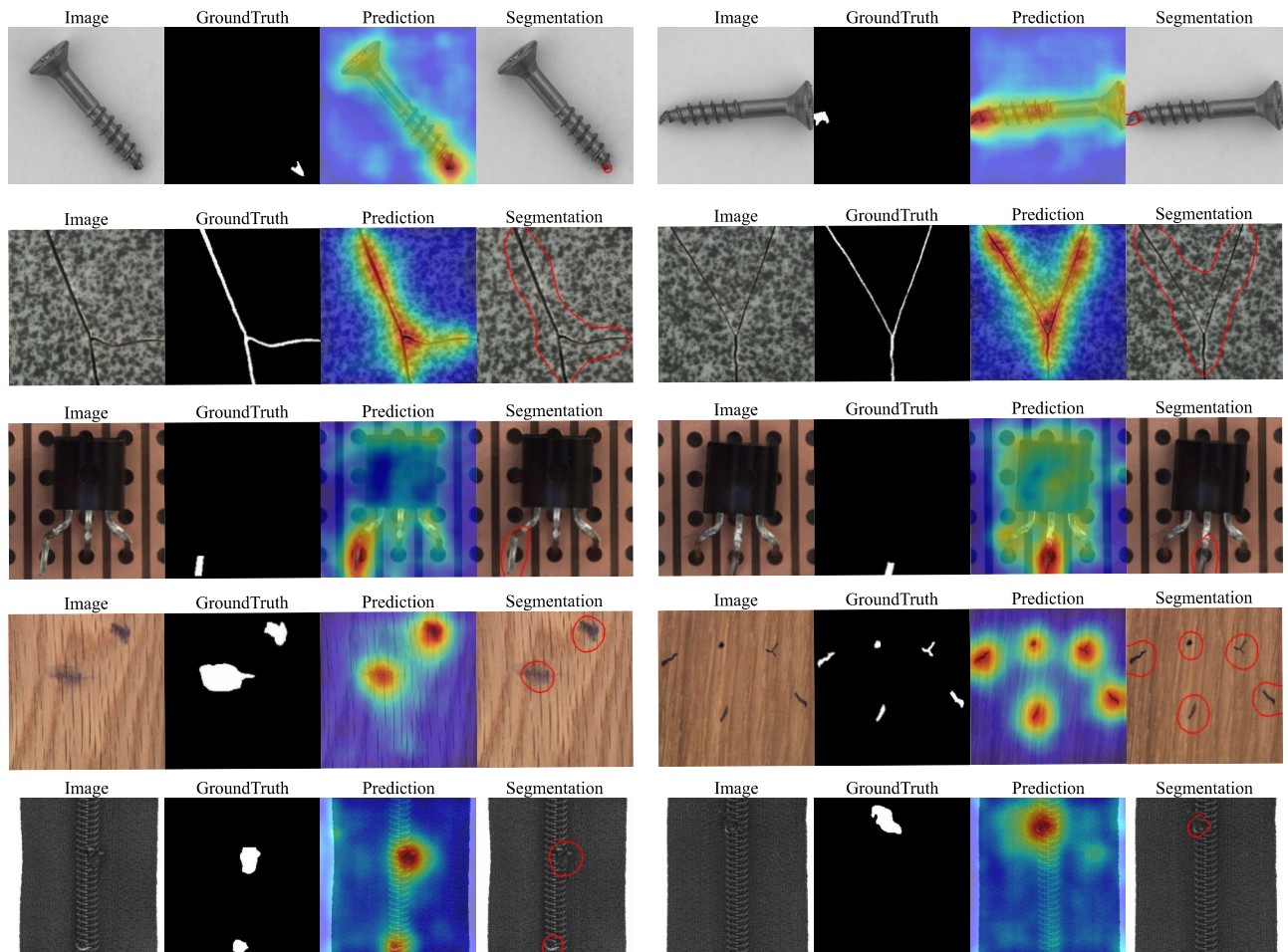


Figure S3: Visualization of 6 categories of MVTec AD: screw, tile, transistor, wood and zipper.

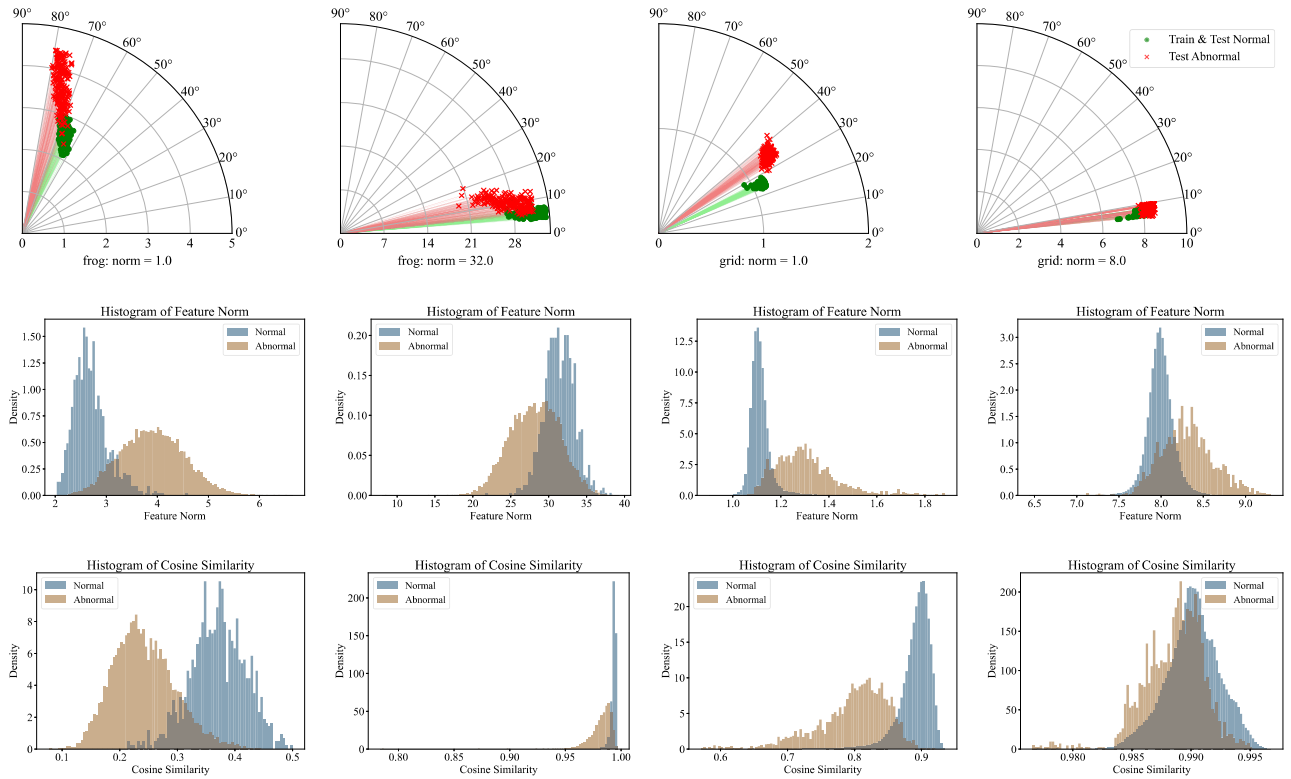


Figure S4: Inappropriate norm of OCC’s optimization objective can lead to significant degradation of detection performance. Here are two examples for the frog category (first two columns) in CIFAR10 and the grid category (last two columns) in MVTec AD. For the frog category, the image-level average ROC AUC decreases from 95.8% (norm=1.0) to 92.7% (norm=32.0). The cosine similarity between positive and negative samples also becomes more indistinguishable at norm=32.0. A similar trend was seen in the grid category of MVTec AD, where the image-level average ROC AUC % decreased from 99.6% (norm=1.0) to 75.2% (norm=8.0).

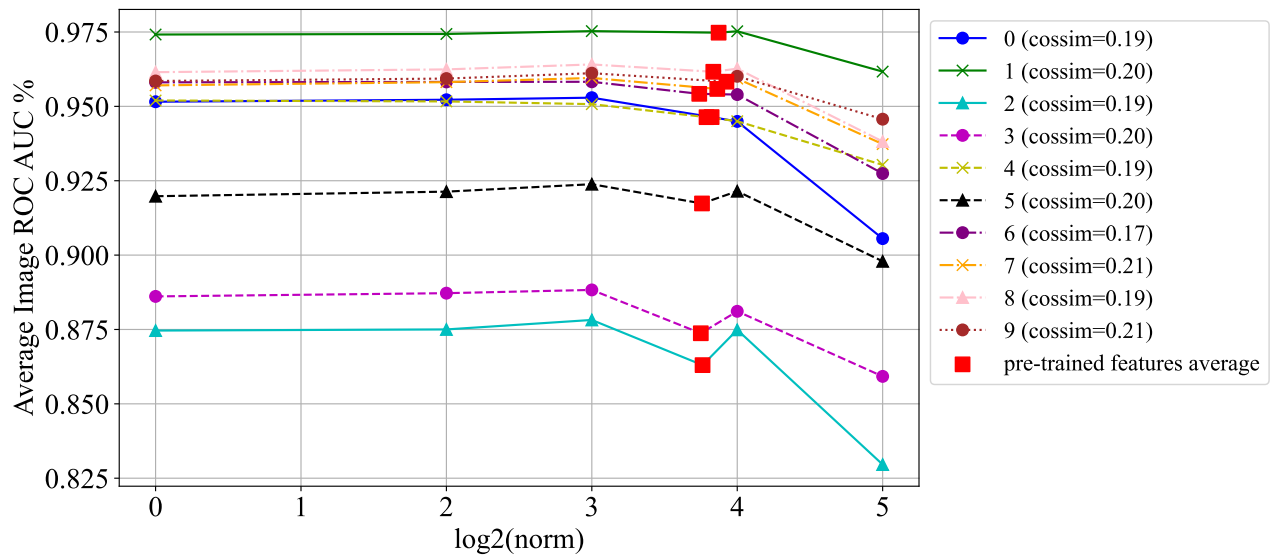


Figure S5: Impact of OCC optimization objective’s norm on each category in CIFAR10.

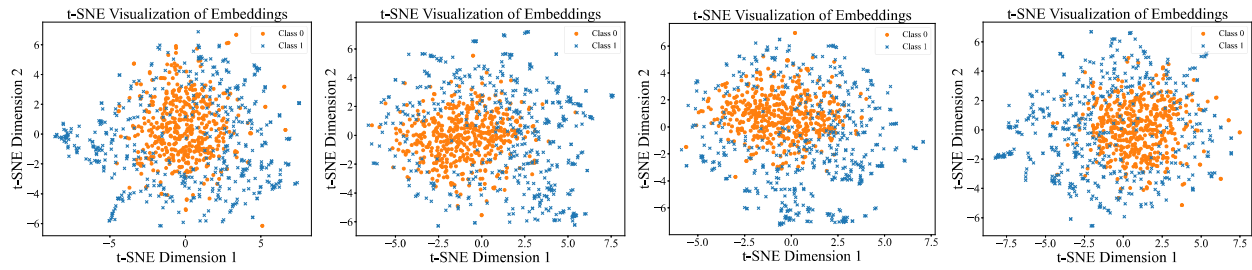


Figure S6: Frog category in CIFAR10. From left to right are the t-SNE plots for the case where the OCC optimization objective obeys the pre-trained features average, standard normal distribution  $\mathcal{N}(0, 1)$ , uniform distribution  $\mathcal{U}(0, 1)$  and  $\mathcal{J}(1)$  with each element is 1, respectively.